Eur. Phys. J. E (2014) **37**: 85
DOI 10.1140/epje/i2014-14085-2

THE EUROPEAN PHYSICAL JOURNAL E

Regular Article

Dimple coalescence and liquid droplets distributions during phase separation in a pure fluid under microgravity

Ana Oprisan[1,a], Sorinel A. Oprisan[1], John J. Hegseth[2], Yves Garrabos[3], Carole Lecoutre-Chabot[3], and Daniel Beysens[4,5]

[1] Department of Physics and Astronomy, College of Charleston, Charleston, SC 29424, USA
[2] Department of Physics, University of New Orleans, New Orleans, LA 70148, USA
[3] CNRS, Univ. Bordeaux, ICMCB, ESEME, UPR 9048, F-33600 Pessac, France
[4] Service des Basses Temperatures, CEA-Grenoble et Universite Joseph Fourier, Grenoble, France
[5] Physique et Mecanique des Milieux Heterogenes, UMR 7636 CNRS - ESPCI - Universite Pierre et Marie Curie - Universite Paris Diderot, 10 rue Vauquelin, 75005 Paris, France

Received 23 March 2014 and Received in final form 14 August 2014
Published online: 30 September 2014 –

Abstract. Phase separation has important implications for the mechanical, thermal, and electrical properties of materials. Weightless conditions prevent buoyancy and sedimentation from affecting the dynamics of phase separation and the morphology of the domains. In our experiments, sulfur hexafluoride (SF_6) was initially heated about 1 K above its critical temperature under microgravity conditions and then repeatedly quenched using temperature steps, the last one being of 3.6 mK, until it crossed its critical temperature and phase-separated into gas and liquid domains. Both full view (macroscopic) and microscopic view images of the sample cell unit were analyzed to determine the changes in the distribution of liquid droplet diameters during phase separation. Previously, dimple coalescences were only observed in density-matched binary liquid mixture near its critical point of miscibility. Here we present experimental evidences in support of dimple coalescence between phase-separated liquid droplets in pure, supercritical, fluids under microgravity conditions. Although both liquid mixtures and pure fluids belong to the same universality class, both the mass transport mechanisms and their thermophysical properties are significantly different. In supercritical pure fluids the transport of heat and mass are strongly coupled by the enthalpy of condensation, whereas in liquid mixtures mass transport processes are purely diffusive. The viscosity is also much smaller in pure fluids than in liquid mixtures. For these reasons, there are large differences in the fluctuation relaxation time and hydrodynamics flows that prompted this experimental investigation. We found that the number of droplets increases rapidly during the intermediate stage of phase separation. We also found that above a cutoff diameter of about 100 microns the size distribution of droplets follows a power law with an exponent close to −2, as predicted from phenomenological considerations.

1 Introduction

Classically, quenching fluids, *i.e.* imposing a rapid temperature drop, leads to phase separation either via nucleation or spinodal decomposition. During nucleation, the new liquid or vapor minority phase needs to overcome the energy cost of vapor-liquid surface formation and is characterized by metastability [1,2]. On the other hand, during spinodal decomposition, the system's susceptibility is negative, the density fluctuations are unstable and grow to ultimately reach the vapor and liquid composition. However, in the vicinity of a critical point, large density fluctuations occur, which makes the above mean-field approaches inadequate [3]. During generalized nucleation, the new phase emerges from critical density fluctuations. The newly formed domains interact with each other by collisions-induced coalescence (CIC). For low volume fraction, *i.e.* large separation distances among droplets, collisions occur due to Brownian motion. For large volume fraction, *i.e.* short separation distances among droplets, hydrodynamic interactions among droplets dominate. As a result, for low volume fraction, the phase separation pattern consists of isolated droplets, whereas at large volume fraction interconnected patterns called "interconnected decomposition" occur, which are reminiscences of a spinodal decomposition pattern. Moreover, the presence of solid walls and the wetting effects dramatically modify phase separation dynamics [4–7]. Both phase separation and critical wetting phenomena were studied almost independently and it has been shown that these two non-equilibrium phenomena could be coupled [8]. Wetting dynamics is coupled with phase separation that takes place

[a] e-mail: oprisana@cofc.edu

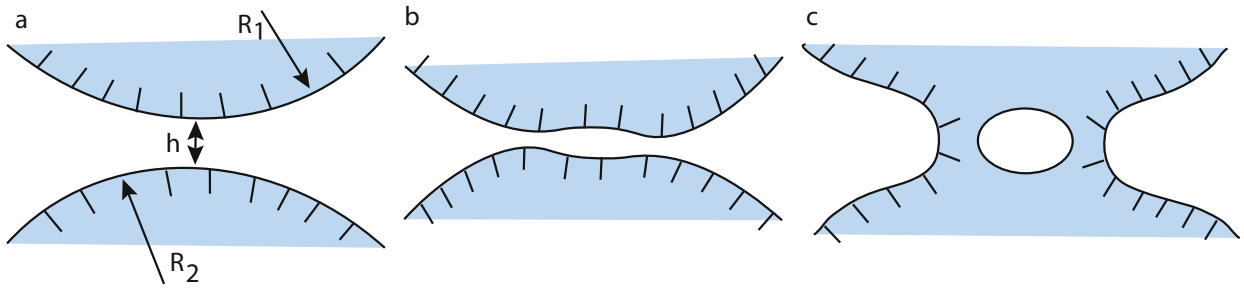

Fig. 1. Cross-sections of liquid droplets of radii R_1 and R_2 that form a thin film ($h \ll R_1, R_2$) (a). The drainage of the thin film and the competing viscosity effects lead to the thinning of the film and the formation of a dimple (b). When the minimum film thickness reaches a critical value, the film rupture occurs and leads to the formation of a larger droplet that traps inside a small bubble (c).

in the bulk of the fluid. It was shown that in the case of liquid droplet-forming phase separation, the wetting speed is much smaller than in the case of bi-continuous phase separation [9]. On Earth, gravity induces collisions between the gas bubbles (the liquid droplets) that then fuse together when moving upwards (downwards). These coalescences favor the creation of macroscopic gas and liquid homogeneous phases, separated by a horizontal meniscus. As an example, we mention phase separation in two-phase flows [10,11], where the velocity field induced by the merging of two drops entrains other drops, thus enhancing the rate of coalescence. Experiments carried out in microgravity suppress the gravitational coalescence and allow a reasonably long time of observation of the phase-separating liquid droplets [12].

The initial evolution of liquid and vapor domains after nucleation has taken place is due to a diffusion mechanism. The temporal evolution of the characteristic length of the nucleation domains follow a power law with an exponent of 1/2 or 1/3, depending on the initial supersaturating conditions [13]. As described by Lifshitz and Slyozov theory and its extensions [14,15], later stages (LS) of phase separation where the smaller droplets evaporate on larger ones (because their pressure is higher) is also characterized by a growth law with an exponent of 1/3. When the droplets have reached local equilibrium, they interact by CIC mechanism. The volume fraction of the minority phase then determines whether the system follows interconnected decomposition or isolated droplet path [16]. For small volume fractions (less than about 30%), the same growth law exponent of 1/3 was found when coalescence is triggered by Brownian collisions [16–18]. In this regime, the capillary forces are stronger than the lubrication forces and the coalescence occurs after the nucleation of a hole without initial droplets deformation [17]. When the volume fraction is significantly larger (more than about 30%), a collision between two droplets induces another coalescence leading to an avalanche of collisions. As a result, interconnected patterns of liquid and vapor domains occur [16]. When two such interconnected domains ("tubes") approach one another, a thin film forms with the minimum thickness at the center (fig. 1a). The growth of tubes is due to the local motion of the two tubes [17] or droplets [19]. As the tubes come closer, the rate of thinning of the thin layer between them decreases due to increased viscous resistance as the film becomes thinner [20]. Such an increase in the viscous resistance gives rise to a local radial pressure gradient that leads to the formation of a dimple (see fig. 1b). The presence of a dimple can lead to film rupture on the rim surrounding the dimple [21–23] and the formation of a large droplet that contains an inner bubble (fig. 1c). Two parameters determine whether the dimple leads to film rupture and the formation of a larger liquid droplet with a small gas bubble inside: the coalescence time and the critical thickness of rupture [24,25]. The main difficulties in the theoretical and experimental investigations of dimple coalescence are due to the presence of the thin film whose thickness can be 4-5 orders of magnitude smaller than the global scale, *i.e.* droplet radii in fig. 1a. Because of this large spatial scale difference between the macroscopic droplets and the molecular-level thin film, the existing experimental measurements fail to supply any information about the evolution of the film profile and its thickness [26–28]. A second experimental difficulty resided in the very short time scale of the film rupture during dimple coalescence [29–31]. As it was shown by Kendon *et al.* [32], who used large scale numerical simulation of coarsening processes taking place during spinodal decomposition in binary mixtures, the "pinchoff" and "topological reconections" of domains of the same phase must "occur rapidly enough not to impede the coarsening process". As a result of the very short temporal and spatial scales of film rupture during dimple coalescence, we were only able to find indirect evidences of such phenomenon during droplet collision. While at a 24 frames/s recording rate we were not able to capture the film rupture and offer direct evidences in support of dimple coalescence, we were still able to capture separate droplets coming closer and closer to each other and then the resulting larger droplet that contains a small, yet visible, gas bubble trapped inside, which represents the memory of the dimple coalescence.

Thus far, dimple coalescences were only observed in density-matched binary liquid mixture near its critical point of miscibility [17]. Here we present experimental evidences that suggest a possible dimple coalescence mechanism in pure, supercritical, fluids of low viscosity under microgravity conditions. Although both liquid mix-

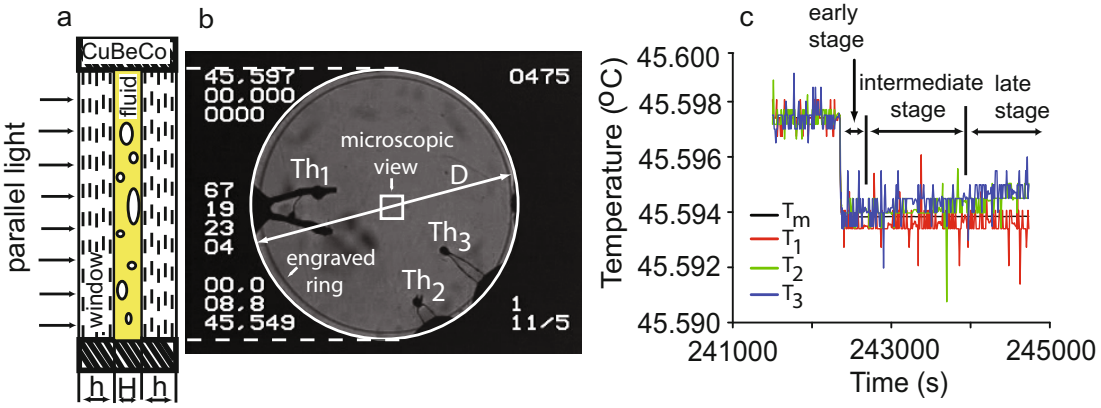

Fig. 2. (a) A sketch of the cross-section of the cylindrical sample cell unit (SCU). The pure fluid (SF_6) of thickness $H = 4.34\,\text{mm}$ is contained between two identical sapphire windows of thickness $h = 9\,\text{mm}$ and a CuBeCo alloy ring (not to scale). (b) A macroscopic (full view) image of the SCU shows the locations of the three thermistors (Th1, Th2, Th3), the reference engraved ring and the location of the $0.9\,\text{mm} \times 0.9\,\text{mm}$ microscopic view window. (c) The temperature profile measured by the three thermistors plus the temperature reading T_m of a thermistor embedded in the alloy housing shows the last 3.6 mK quench that leads to phase separation.

tures previously studied in [17] and pure fluids belong to the same universality class, both the mass transport mechanisms and their thermophysical properties are significantly different. For example, in supercritical pure fluids, the transport of heat and mass are strongly coupled by the enthalpy of condensation, whereas in liquid mixtures mass transport processes are purely diffusive. Furthermore, the viscosity η is also much smaller in pure fluids than in liquid mixtures. For these reasons, there are large differences in the fluctuation relaxation time and hydrodynamics flows that prompted this experimental investigation of a possible dimple coalescence mechanism in pure fluids. We present indirect experimental evidences of dimple coalescence in SF_6, which was unexpected due to a smaller viscosity (by a factor of 10) compared to binary mixtures. In summary, this study brings two novel findings: 1) we suggest that there are indirect experimental evidences of dimple coalescence processes in pure fluids near critical point in microgravity during the intermediate stage of phase separation, and 2) we showed that the long tail of the experimentally determined distribution of droplet diameters obtained both from macroscopic and microscopic images follow a power law with an exponent of -2, as predicted from phenomenological considerations.

2 Experimental setup

A cylindrical cell filled with SF_6 of 99.98% purity (from Alpha Gaz - Air Liquide), was placed inside a copper sample cell unit (SCU), which in turn was placed inside a thermostat (not shown, see [33] and references therein). A thin layer of epoxy sealed the sapphire windows to the copper encasing and decreases the thermal conductance between the window and the copper. The interior diameter of the copper cylindrical cell was $D = 12\,\text{mm}$ with a 10 mm circle engraved on one of the sapphire windows. The thickness of each sapphire windows was $h = 9\,\text{mm}$, and the thickness of the SF_6 layer was $H = 4.34\,\text{mm}$ (fig. 2a, not to scale). The aspect ratio of this cell $\Gamma = D/H = 2.765$ was large enough to allow the gas bubbles grow to a large size without significant limiting effects due to the wetting that occurs between the bubble and the walls. The fluid inside the SCU was prepared at the critical density, *i.e.* $\langle \rho* \rangle = (\langle \rho \rangle - \rho_c)/\rho_c = \pm 0.02\%$, where $\langle \rho \rangle$ is the mean density and ρ_c is the critical density [34] (see also [19,33, 35–39] for more details regarding the microgravity setup used in our experiments).

For this experiment, we used direct imaging capabilities of Alice 2 - CNES facility in order to record density fluctuations near critical point of SF_6 in microgravity. Alice 2 instrument is a compact optical, thermal, and mechanical facility operating a thermostat of very accurate thermal regulation, allowing $10\,\mu\text{K}$ of relative temperature accuracy and $40\,\mu\text{K/h}$ of temporal stability, in the range of 30 °C to 60 °C. The droplets in the full view field of the cell were visualized through light transmission normal to the windows using a monochromatic He-Ne laser with $\lambda = 632.8\,\text{nm}$ of about 1 mW maximum power. Laser stability after 1 h was estimated to be better than 0.3% [38]. For calibration purposes, the diameter of the 10 mm circle engraved on the sapphire window was matched to approximately 210 pixels, leading to a resolution of approximately $47.6\,\mu\text{m/pixels}$ in all full view images. A microscope objective with $15\times$ magnification periodically focuses on a $0.9\,\text{mm} \times 0.9\,\text{mm}$ square at the center of the SCU and produces detailed (microscopic) views (fig. 2b). Based on our calibration, a 0.9 mm line in the microscopic view corresponded to 288 pixels, leading to a resolution of approximately $3.1\,\mu\text{m/pixel}$ [36]. The set of four digits located in the central left side of the SCU view (fig. 2b) represents the recording time. The fluid was held at a constant

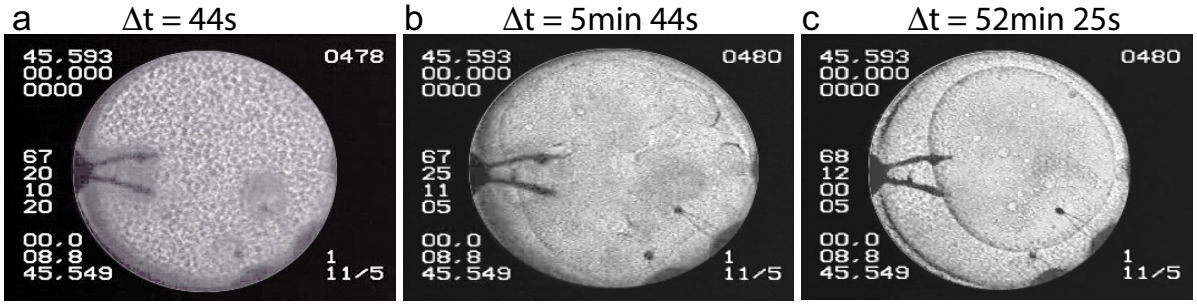

Fig. 3. Macroscopic views of the SCU. Interconnected domains are characteristic of the ES phase separation. (a) Darker regions correspond to the wetting layers formed around the three embedded thermistors. (b) The wetting layer between the copper wall and the large gas bubble forms and quickly grows during the IS. The number of droplets grows very fast due to coalescences between domains. (c) During the LS, the wetting layer surrounding the large gas bubble is almost constant and liquid droplets continue to occur inside the large gas bubble. The relative time Δt is measured from the last 3.6 mK temperature quench that produced phases separation.

initial temperature of about 1 K above critical temperature for about 40 minutes. Subsequently, the protocol was repeated by decreased fluids temperature using at last a 3.6 mK quenches until the fluid crossed its critical temperature and phase-separated (see [39,33,19] for additional details regarding the experimental setup). For the image shown in fig. 2b, the time was 67 hours, 19 minutes, 23 seconds, and 4/24 fractions of a second, *i.e.* an absolute time approximately equal to $t = 242363$ s. Instead of using the above absolute time stamp marked on recorded images, only the relative time $\Delta t = t - t_{\text{quench}}$ was used throughout the rest of the paper. Here, $t_{\text{quench}} = 242366$ s is the time stamp of the last 3.6 mK quench during which the fluid crossed its critical temperature and phase-separated.

3 Results

We divided the time interval from the moment the thermal quench was applied until the end of phase separation in three stages. The early stage (ES) of phase separation starts at about $\Delta t = 23$ s and ends at about $\Delta t = 345$ s lasting about 5 minutes (fig. 2c). The ES is characterized by interconnected domains of the same phase (fig. 3a), which is a characteristic of fast growth processes consistent with the universal curve [12,33]. The intermediate stage (IS) spans the time interval between $\Delta t = 345$ s and $\Delta t = 605$ s, *i.e.* the next approximately 5 minutes. During the IS, a wetting layer appears and quickly grows between the wall of the sample cell unit (SCU) and the gaseous phase (fig. 3b). Indirect evidences of dimple coalescence in the form of large droplets that occupy the same spatial location of two smaller and very close droplets with a small gas bubble trapped inside were found during this IS. The droplets distribution growth is fast until the wetting layer separates the large gas bubble from the walls. We previously found a power law exponent of 0.39 ± 0.01 for the growth of the average thickness of the wetting layer [19]. During the late stage (LS) of phase separation, the thickness of the wetting layer is almost constant (fig. 3c).

3.1 Droplet coalescence in the intermediate stage of phase separation

We analyzed over 110 minutes of microgravity recordings and found indirect evidences of dimple coalescences as seen in fig. 4 in the form of small gas bubble trapped inside a large droplet resulted from the collision of two smaller droplets. The sequence of snapshots in fig. 4 follows the coalescence between approaching interfaces. Figure 4 shows a representative subset of successive images that capture droplet coalescences at different stage. In fig. 4a1 we identified three regions of interest (ROIs). The first ROI is marked with a solid white square and contains two almost spherical regions vertically aligned near the dark tip of the thermistor Th1 (upper left side of the macroscopic image). The white arrow inside the solid white square points approximately to the midpoint between the two droplets in contact. The second ROI is marked with a dashed white square that includes a small portion of two dark parallel interfaces, about 1 mm long (see the upper right corner of the dashed square). The white arrow is parallel to the narrow space between the two parallel dark interfaces. The third ROI is marked with a dashed-dotted white square that also includes a small portion of an interfaces (dark straight line indicated by the white arrow). The white arrow points towards two small droplets at the interface (dark line). In the first ROI (solid white square), over about five minutes, a large droplet (see fig. 4b1) takes the place of the two small droplets from fig. 4a1. The direction of the white arrows approximates the direction of the fluid element displacement inside the large gas bubble. We visually identified ROIs where CIC occurred and subsequently used intensity profile lines to quantitatively check our results (see below). For example, from the first ROI (solid white square) in fig. 4a1, we cut and magnified the area around the two droplets in contact with each other (see the inset in fig. 4a2). We drew a vertical profile line from the bottom to the top and a horizontal profile line from the left to the right side of the magnified inset shown in fig. 4a2. The distance along the profile line is measured in percent of the 17 pixels (1 pixel

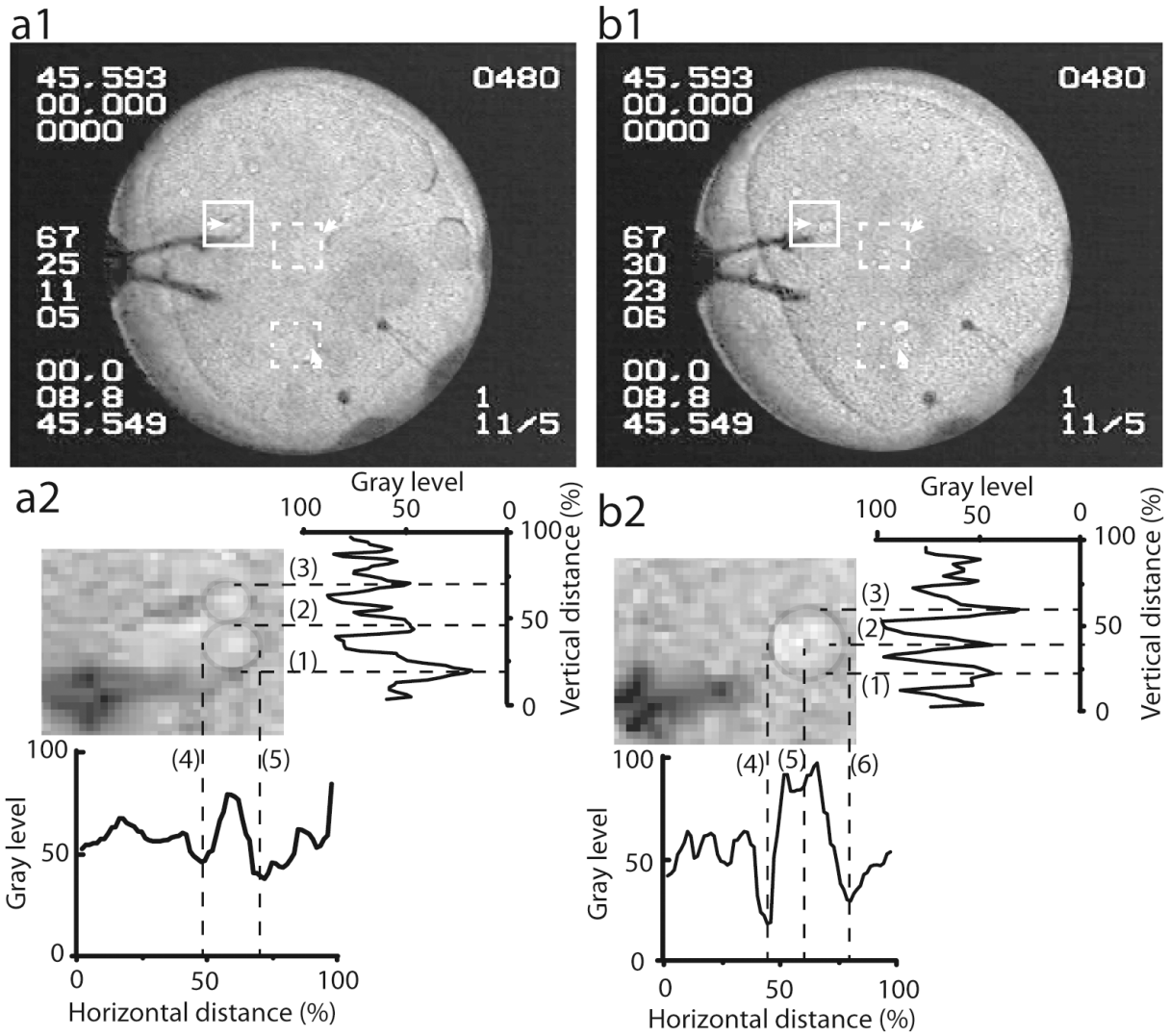

Fig. 4. Coalescences of interfaces take place during the intermediate stage of phase separation and lead to the formation of larger droplets. Three different regions of interest (ROIs) were followed. In the first ROI (solid white square), two small droplets came very close to each other (a1) and through dimple coalescence mechanism they produced a larger spherical droplet (b1) with a small gas bubble trapped inside. The white arrow points to the actual droplets and, at the same time, approximately follows the direction of the macroscopic flow inside the large gas bubble. In the second ROI (dashed white square), two dark parallel interfaces almost 1 mm long came close to each other (a1) and eventually led to the formation of three droplets (b1). In the third ROI (dashed-dotted white square), two small bubbles at the dark interface (a1) eventually led to a large droplet in panel b1. Both the vertical and horizontal intensity profile lines through the magnified insets of the first ROI (panels a2 and b2) identify dark boundaries (low intensity) of droplets during the coalescence. The white squares are 17 pixel wide. The distance along the intensity profile line is measured in percent of the 17 pixel side of the white square.

$= 47.6\,\mu$m) represented by the side of the white square shown in fig. 4a1. The boundary of the ROI gave a high gray level intensity (white corresponds to gray level intensity of 255) whereas dark regions, such as the boundaries of the droplets, produced low gray level intensities (black corresponds to gray level intensity of zero). A vertical section through the two almost vertically aligned droplets seen in the first ROI of fig. 4a1 and the corresponding magnified inset shown in fig. 4a2 clearly identifies a dark boundary (low gray level intensity) when crossing into the first droplet (dashed line "(1)"), a second dark and wider boundary between the two droplets (dashed line "(2)"), and finally a similar dark region when transiting out of the second droplet (dashed line "(3)"). Similarly, a horizontal section through the bottom droplet seen inside the solid white square in fig. 4a1 and the corresponding magnified inset of fig. 4a2 identifies a dark boundary when crossing into the droplet (dashed line "(4)") and another dark boundary when crossing out of the same droplet (dashed line "(5)").

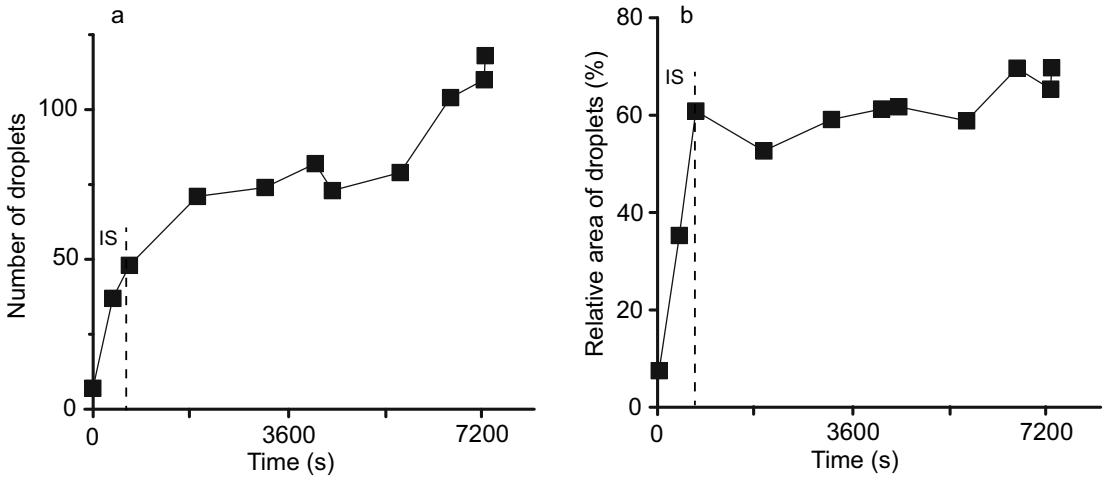

Fig. 5. (a) The number of liquid droplets increases rapidly during the intermediate (IS) stages of the phase separation. (b) The relative area of the droplets (in cross-section) with respect to the area of large gas bubble that includes them (see fig. 3c and fig. 4 for clearly visible boundaries of the large gas bubble inside the SCU) also increases rapidly during the intermediate stages of phase separation.

The coalescence in the first ROI terminates in a larger droplet (see fig. 4b1), which represents the memory of this mode of coalescence. The small dark spot at the center of the large liquid droplet formed after coalescence (see the magnified inset in fig. 4b2) is a small gas bubble that was trapped between the two colliding interfaces. The second ROI (dashed white square) shows the evolution of two parallel interfaces which after collision end up in a series of droplets (fig. 4b1). Similarly, the third ROI (dashed-dotted white square) followed the evolution of two small droplets (fig. 4a1) at the dark interface, which subsequently evolved into two larger droplets at the same interface (fig. 4b1). Dimple coalescences occur only throughout the IS phase separation and ended when a macroscopic bubble has formed, *i.e.* during the late stage. The coalescences dominate the intermediate stage of phase separation and lead to a rapid increase in the number of liquid droplets (see fig. 5a). During most of the late stage the number of droplets is almost constant, suggesting that probably the system reached a quick dynamic equilibrium. The relative area of the droplets to the area of the gas bubble that encloses them rapidly increases during the IS and then is almost constant throughout most of the late stage (see fig. 5b). The sharp increase in the number of droplets towards the end of the LS and a corresponding modest increase of the surface area of the droplets suggests that the added droplets are mostly of small diameter.

In order to more clearly emphasize the characteristics of the temporal evolution of the distributions, we followed different size bins over time both in macroscopic (fig. 6a) and microscopic (fig. 6b) images. In macroscopic view (fig. 6a), the histograms used a one-pixel bin (1 pixel $= 47.6\,\mu$m). We found that 30% of the droplets are 4-5 pixels in diameter (see the solid rhombs in fig. 6a) and about 60% of that are 2-3 pixels in diameter (see the solid triangles in fig. 6a). We also noticed that although fluctuations in the fraction of droplets are present in (at least) certain bin sizes due to collisions, the averages of the distributions for each bin size are relatively stable. This observation suggests that the distributions reached probably a stationary state during the late stage of phase separation (see fig. 6a). Furthermore, we noticed that a momentary increase in the population of 4-5 pixel-diameter droplets around $\Delta t = 4134\,$s is accompanied by a decrease in the population of the 2-3 pixel droplets suggesting that coalescence processes preserve the volume fraction of droplets.

For the temporal evolution of the distributions of droplet diameters in microscopic views (fig. 6b), we used bins of 15 pixels in order to match the macroscopic view bins (since the magnification factor is 15×). We noticed the same characteristics of the droplet distributions as in the macroscopic views: 1) the averages of the fraction of droplets is relatively constant over time, which suggests that the droplet size distributions could be stationary, and 2) the equilibrium attained during phase separation is dynamic and fluctuations in the fraction of droplets compensate each other in order to preserve the total volume fraction of the droplets. For example, a steady decline in the fraction of droplets with diameter of 0–15 pixels (see solid squares in fig. 6b) is compensated by an increase in the fraction of droplets with 30–45 pixels in diameter (solid triangles in fig. 6b).

3.2 Distribution of droplet diameters

Both for the macroscopic (fig. 7a1) and microscopic (fig. 7b1) images the corresponding average droplet size distributions (fig. 7a2 and 7b2) were obtained by measuring the droplet diameters with iSolutionTM software. Previous theoretical predictions of the bubble size distribution during coalescence in turbulent flows suggested that a realistic distribution function is lognormal [40]. Experiments performed with gas bubbles in turbulent water under microgravity conditions during parabolic flights aboard the

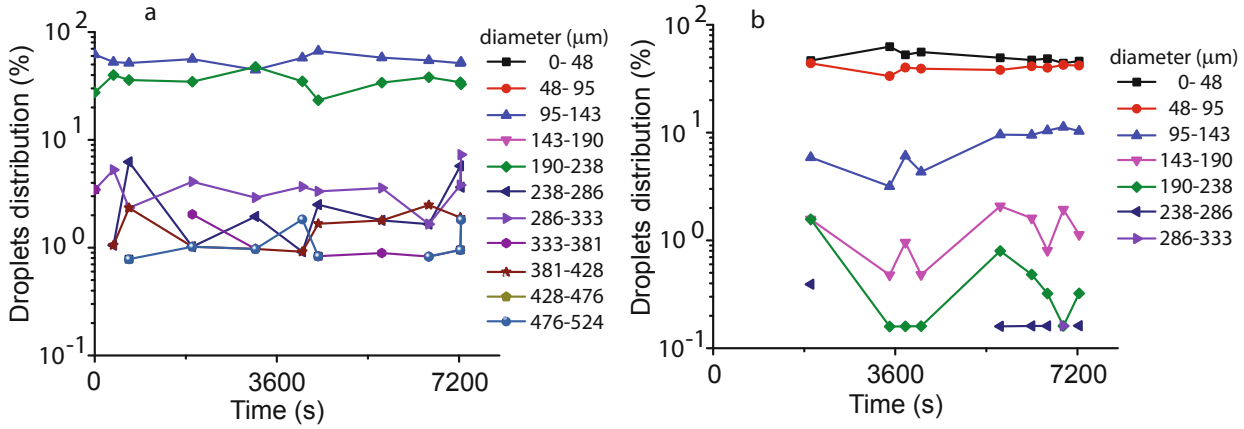

Fig. 6. Temporal evolution of the distribution of liquid droplet diameters (in pixels) for macroscopic (a) and microscopic (b) views. In macroscopic views the bin size was set to one pixel whereas in microscopic view the bins were 15 pixels and matches the magnification of the microscope. Two characteristics of the distributions are common both for the macroscopic and the microscopic views: 1) the averages of the fraction of droplets are relatively constant over time (stationary distributions), and 2) the equilibrium attained during phase separation is dynamic with brief fluctuations that compensate each other across different bin sizes in order to preserve the total volume fraction of the droplets.

Caravelle "ZERO-G" aircraft also suggested that the best fit of bubble distribution is lognormal [41].

As we explained elsewhere (see [19,33]), due to the growth of the liquid layer between the copper wall and the gas bubble, there is a small-amplitude periodic motion of the entire gas bubble inside the SCU. The amplitude of the fluid displacement depends on the distance from the instantaneous center of rotation, which is close to the center of the SCU. For example, since the microscope is always pointing at the center of SCU that almost coincides with the center of instantaneous rotation, the fluid displacement has a small amplitude of about 0.3 mm. Although convective fluid displacement is present in our experiment, its amplitude and velocity (see [19,33]) are far from the turbulent flow imposed in [41]. Nonetheless, it seems that average droplet size distributions both for macroscopic (fig. 7a2) and the microscopic (fig. 7b2) images in our experiments could also be fitted to a lognormal function. However, the center of the macroscopic distribution (fig. 7a2) is at about 180 μm and that of the microscopic distribution (fig. 7b2) is at about 40 μm, which means that they do not scale by the microscope's magnification factor of 15. A possible explanation for such a mismatch is the violation of the spatial ergodicity requirement. As we noticed from fig. 2b, the microscopic view is a 0.9 mm $\times$ 0.9 mm window always focused at the center of the SCU. For comparison, the engraved ring on the sapphire window that is visible in all macroscopic images has a diameter of 10 mm. As a result, the microscopic views only sample a very small area that represents about 0.7% of the total area of the macroscopic view. For the centers of the two distributions to scale exactly by the microscope magnification factor of 15, we would have to move around the microscope to ensure equal probability of sampling every region of the macroscopic view. Only under such circumstances the center of the microscopic distribution multiplied by the magnification factor of the microscope would match the center of the macroscopic distribution. However, in our experiment we always sampled only the center of the SCU. As a result, we would not expect the centers of the microscopic and macroscopic distributions to coincide.

While at small diameters, below 100 μm, the size distribution statistics is very poor in macroscopic images due to measurements done close to the resolution limit of 1-2 pixels, the statistics is significantly better at large diameters (above 100 μm). Furthermore, the macroscopic and microscopic size distributions overlap in the range 100 to 300 μm (see the shaded rectangle in fig. 7b1 that represents the range of diameters measured in microscopic images).

For large droplet diameters, Beysens *et al.* [17] used dimensional analysis consideration and derived a quantitative relationship for the bubble sizes distribution. In their derivation, only binary interactions (collisions) between domains ("tubes" or droplets) were considered and the rate of change of the number of domains was estimated as $\mathrm{d}N/\mathrm{d}t = -N^2 \int_\Sigma p(r)\mathbf{V}\cdot\mathbf{n}\mathrm{d}\Sigma$, where N is the number of domains per unit volume, $p(r)$ is the pair distribution function of the tubes, $\mathbf{V}$ is the relative velocity of the tubes, and $\mathbf{n}$ is the outward normal to the collision surface Σ. They found that the long tail of the droplet size distribution, such as those found in both our macroscopic (fig. 7a2) and microscopic (fig. 7b2) images can be reasonably modeled mathematically for radii over a natural cutoff with a power law, *i.e.* $\mathrm{d}N(r)/\mathrm{d}r = Ar^\theta$. In their experimental work, the range of power law exponent θ was between 1.5 and 2.9 [17]. Martula *et al.* [10] also assumed a binary collision mechanism for CIC similar to the approach of [17]. The phenomenological rate equation of CIC is $\mathrm{d}N/\mathrm{d}t = -kN^2$ and uses a dimensional analysis based coefficient k to arrive at the conclusion that a possible solution is $N(r) = \frac{3\phi}{4\pi}r^{-3}$, where ϕ is the volume fraction of the minority phase [10]. They carried out molecular dy-

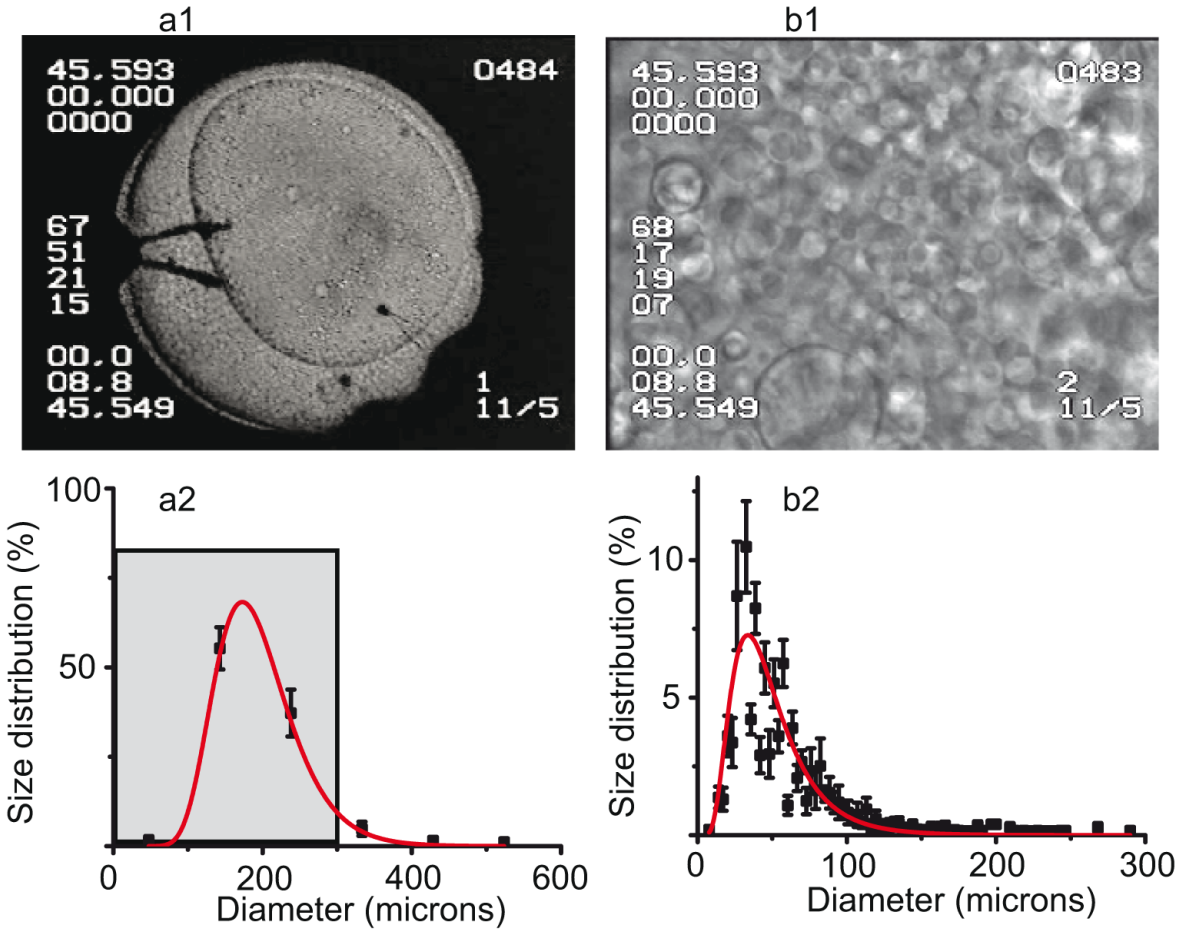

Fig. 7. (a1) A macroscopic view image shows liquid droplets formed inside a well-defined large, off-center, gas bubble. (a2) The size distributions of droplets with a bin size of 1 pixel (47 microns) from multiple macroscopic images were averaged and fitted with a lognormal distribution (continuous line). (b1) A microscopic view obtained with a 15× magnification microscope reveals a densely packed section with droplets. (b2) The size distributions of droplets with a bin size of 15 pixel (to match the macroscopic bin size) from multiple microscopic images were averaged and fitted with a lognormal distribution (continuous line). The shaded rectangle in panel a2 represents the range of size distributions covered by the microscopic distributions shown in panel b2. The statistics of the size distributions is relevant and overlap for diameters between 100 and 300 microns.

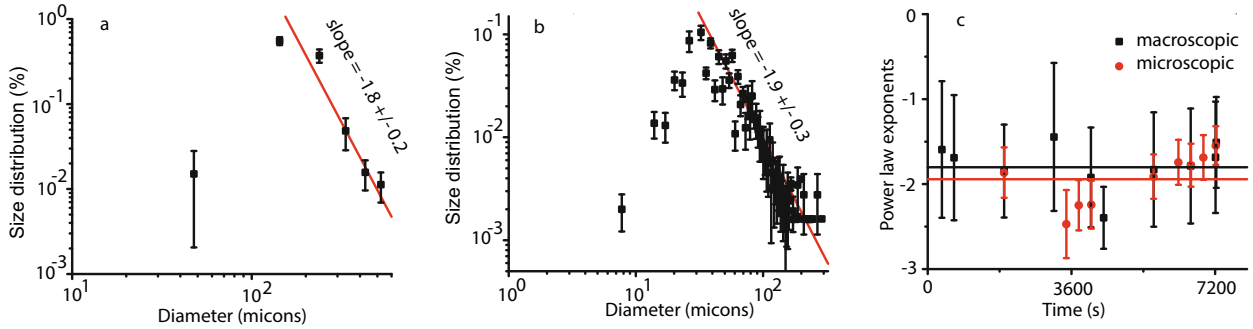

Fig. 8. Power law exponents for the long tail of the average size distribution of droplets in macroscopic (a) and microscopic (b) images. The average value of the exponent is -1.8 ± 0.2 for macroscopic and -1.9 ± 0.3 for microscopic images. The power law exponents of the long tails of the size distributions at different times during the experiment fluctuate around the corresponding averages (c).

namic simulations and found out that, for a large volume fractions of the minority phase, the distribution of droplets *versus* their corresponding diameters becomes wider over time (see fig. 10b in [10]). Their numerical observations are in agreement with our previous results based on microgravity experiments (see fig. 4 in [19]).

Following Beysens *et al.* [17], we also searched for a possible power law at large values of the droplet sizes (see fig. 8). For this purpose, we plotted the macroscopic (fig. 8a) and microscopic (fig. 8b) size distributions on log-log scales. It is apparent that for large diameters (above $100\,\mu$m), the macroscopic (fig. 8a) average size distribution can be fitted with a power law with an average exponent of -1.8 ± 0.2 and the microscopic (fig. 8b) average size distribution can also be fitted with a power law with an average exponent of -1.9 ± 0.3. In addition to the power law fits to the average distributions, we also show power law exponents for individual size distributions at different times during the experiment (fig. 8c). The continuous horizontal lines represent the average values of the power law exponents.

Our results are in agreement with the theoretical predictions [10,17] and experimentally verified values for density-matched liquid mixtures under near-critical conditions [17].

4 Conclusions

In this paper we analyzed the dynamics of the liquid droplets formation inside the gaseous phase of a pure fluid during the intermediate and late stages of the phase separation process under microgravity. We bring indirect experimental evidence in support of the so far unobserved dimple coalescences in pure fluids under microgravity. These results are unexpected due to a large difference between the viscosity of pure fluid that is much lower than the viscosity of a binary mixture.

We determined the distributions of the diameters of the liquid droplets both from macroscopic and microscopic views. The size distributions seem to fit the lognormal distribution as predicted theoretically by [40,42].

Due to poor statistics of measurements near the resolution limit of images (below $100\,\mu$m) we focused on deriving quantitative measures from both the macroscopic and microscopic data for large droplet diameters (above $100\,\mu$m). Our results show that a power law with an exponent close to -2 is a good fit for both the macroscopic and microscopic size distributions. Although a similar value for the power law exponents was previously obtained from microgravity experiments with binary mixtures [17], this is the first report on such a regime in pure fluids that are known to have a much lower viscosity (by an order of magnitude smaller than binary mixtures). Additionally, the power law exponents we found are in good agreement with the theoretically predicted value from phenomenological considerations [10,17].

This research was supported by a Research and Development grant from the College of Charleston to A. Oprisan. The National Science Foundation IOS CAREER award 1054914 is acknowledges by S.A. Oprisan. Experimental work was supported by NASA Grants NAG3-1906 and NAG3-2447 to J.J. Hegseth. D. Beysens, Y. Garrabos and C. Lecoutre-Chabot acknowledge CNES support.

References

1. W. John Cahn, E. John Hilliard, J. Chem. Phys. **29**, 258 (1958).
2. J.W. Cahn, J.E. Hilliard, J. Chem. Phys. **31**, 688 (1959).
3. K. Binder, *Spinodal Decomposition*, Vol. **5**, Sect. 7, *Phase Transformations in Materials* (VCH Verlagsgesellschaft, Weinheim, 1991) pp. 405–471.
4. D. Fenistein, D. Bonn, S. Rafai, G.H. Wegdam, J. Meunier, A.O. Parry, M.M. Telo da Gama, Phys. Rev. Lett. **89**, 096101 (2002).
5. P. Guenoun, D. Beysens, M. Robert, Phys. Rev. Lett. **65**, 2406 (1990).
6. Reinhard Lipowsky, David A. Huse, Phys. Rev. Lett. **57**, 353 (1986).
7. Ullrich Steiner, Jacob Klein, Phys. Rev. Lett. **77**, 2526 (1996).
8. H. Tanaka, T. Araki, Europhys. Lett. **51**, 154 (2000).
9. Daniel Bonn, Emanuel Bertrand, Jacques Meunier, Ralf Blossey, Phys. Rev. Lett. **84**, 4661 (2000).
10. D.S. Martula, T. Hasegawa, D.R. Lloyd, R.T. Bonnecaze, J. Colloid Interface Sci. **232**, 241 (2000).
11. D.S. Martula, D.R. Lloyd, R.T. Bonnecaze, Int. J. Multiphase Flow **29**, 1265 (2003).
12. D. Beysens, Y. Garrabos, Physica A **281**, 361 (2000).
13. Andrew Cumming, Pierre Wiltzius, Frank S. Bates, Jeffrey H. Rosedale, Phys. Rev. A **45**, 885 (1992).
14. Celeste Sagui, Dean Stinson OGorman, Martin Grant, Scanning Microsc. **12**, 3 (1998).
15. Celeste Sagui, Martin Grant, Phys. Rev. E **59**, 4175 (1999).
16. Vadim S. Nikolayev, Daniel Beysens, Patrick Guenoun, Phys. Rev. Lett. **76**, 3144 (1996).
17. D. Beysens, P. Guenoun, P. Sibille, A. Kumar, Phys. Rev. E **50**, 1299 (1994).
18. D.A. Beysens, Physica A **239**, 329 (1997).
19. A. Oprisan, J.J. Hegseth, G.R. Smith, Carole Lecoutre, Yves Garrabos, Daniel A. Beysens, Phys. Rev. E **84**, 021202 (2011).
20. I.B. Bazhlekov, A.K. Chesters, F.N. van de Vosse, Int. J. Multiphase Flow **26**, 445 (2000).
21. K.A Burrill, D.R Woods, J. Colloid Interface Sci. **42**, 15 (1973).
22. Q. Deng, A.V. Anilkumar, T.G. Wang, J. Fluid Mech. **578**, 119 (2007).
23. D.S. Dimitrov, I.B. Ivanov, J. Colloid Interface Sci. **64**, 096101 (1978).
24. Derek Y.C. Chan, Evert Klaseboerc, Rogerio Manicac, Soft Matter **5**, 2858 (2009).
25. A.K. Chesters, Chem. Engin. Res. Design **69**, 259 (1991).
26. Y.T. Hu, D.J. Pine, L. Gary Leal, Phys. Fluids **12**, 484 (2000).
27. R. Manica, J.N. Connor, S.L. Carnie, R.G. Horn, D.Y.C. Chan, Langmuir **23**, 626 (2007).

28. R. Manica, E. Klaseboer, D.Y.C. Chan, Soft Matter **4**, 1613 (2008).
29. M.A. Rother, A.Z. Zinchenko, R.H. Davis, J. Fluid Mech. **346**, 117 (1997).
30. John. R. Saylor, Garrett D. Bounds, AIChE J. **58**, 3841 (2012).
31. Y. Yoon, F. Baldessari, H.D. Ceniceros, L.G. Leal, Phys. Fluids **19**, 102102 (2007).
32. V.M. Kendon, M.E. Cates, I. Pagonabarraga, J.C. Desplat, P. Bladon, J. Fluid Mech. **440**, 147 (2001).
33. A. Oprisan, S.A. Oprisan, J.J. Hegseth, Y. Garrabos, C. Lecoutre-Chabot, D. Beysens, Phys. Rev. E **77**, 051118 (2008).
34. P. Guenoun, R. Gastaud, F. Perrot, D. Beysens, Phys. Rev. A **36**, 4876 (1987).
35. D. Beysens, P. Guenoun, F. Perrot, J. Phys.: Condens. Matter **2**, SA127 (1990).
36. J.J. Hegseth, V.S. Nikolayev, D. Beysens, Y. Garrabos, C. Chabot, in *Fourth Microgravity Fluid Physics and Transport Phenomena* (1998).
37. John Hegseth, Ana Oprisan, Yves Garrabos, Vadim S. Nikolayev, Carole Lecoutre-Chabot, Daniel Beysens, Phys. Rev. E **72**, 031602 (2005).
38. C. Lecoutre, Y. Garrabos, E. Georgin, F. Palencia, D. Beysens, Int. J. Thermophys. **30**, 810 (2009).
39. A. Oprisan *Fluctuations, Phase Separation and Wetting Films near Liquid-Gas Critical Point*, Thesis, University of New Orleans (2006).
40. A.M. Kamp, A.K. Chesters, C. Colin, J. Fabre, Int. J. Multiphase Flow **27**, 1363 (2001).
41. Catherine Colin, Xavier Riou, Jean Fabre, Micrograv. Sci. Technol. **20**, 243 (2008).
42. J. Kamp, S. Nachtigall, S. Maa, M. Kraume, Czas. Tech. M **109**, 113 (2012).